Experimental characterization of quasi-2-dimension nanoporous gold ultra-thin film from nano to micro length scale

Julien Godet, Gwénaël Massé, Issraa Shahine, Quentin Hatte, Hadi Bahsoun, Florian Bouard, Loranne Vernisse, Laurent Pizzagalli, Maryline Le Granvalet, Pierre-Yves Tessier

Experimental characterization of quasi-2-dimension nanoporous gold ultra-thin film from nano to micro length scale

Julien Godet[a], Gwénaël Massé[a], Issraa Shahine[b], Quentin Hatte[b], Hadi Bahsoun[a], Florian Bouard[a], Loranne Vernisse[a], Laurent Pizzagalli[a], Maryline Le Granvalet[b], Pierre-Yves Tessier[b]

[a] *Université de Poitiers, ISAE-ENSMA, CNRS UPR 3346, Institut Pprime, Dept of Physics and Mechanics of Materials, 11 Bld. M. et P. Curie, TSA 41123 , Poitiers cedex 9, 86073, France*

[b] *Nantes Université, CNRS, Institut des Matériaux de Nantes Jean Rouxel, IMN , Nantes, F-44000, France*

Abstract

Quasi-2D nanoporous gold ultra-thin films have been elaborated and investigated by specific surface approaches. Three different microscopy techniques (Transmission Electron Microscopy (TEM), Scanning Electron Microscopy (SEM), and Atomic Force Microscopy (AFM)) have been used for the characterizations. A careful statistical analysis of experimental images has been done, thanks to the development of a dedicated image analysis software. It reveals that the inhomogeneous gold nanomesh at low length scale becomes homogeneous at a length scale larger than the biggest pores size of about 2 μm, with a constant opacity reaching 35%. At such a scale, the ligaments present an average diameter of 20 nm and an average length of 70 nm. While TEM and SEM present similar results, AFM overestimates the geometric characteristics due to tip convolution effect. However, the topology of the nanomesh is not affected. This study also reveals pores with a much larger size in the quasi 2D nanoporous ultra-thin film than in its bulk counterpart for similar ligaments diameters, which could play an important role in its mechanical properties.

Keywords: Nano architecture, Transmission electron microscopy, Scanning electron microscopy, Atomic force microscopy, Flexible membrane, Image analysis, Skeletonization

1. Introduction

The surface-on-volume ratio has been identified as one of the main parameters to understand the modification of physical properties at the nano-scale like catalysis or mechanical properties, and used for instance for the famous Ashby diagram [1]. It opened the way to the nano-scale surface engineering that allowed changing the materials properties compared to their bulk counterparts [2]. In addition, the architecture of materials at the nano-scale has been shown to be a key element to improve material properties like the toughness in natural and biological materials [3].

Bulk nanoporous metal [4, 5] is a typical example of such a material combining low dimension and nano-architecture obtained by dealloying processes [6, 7, 8, 9, 10, 11]. In particular bulk nanoporous gold is known for its interesting properties, like catalysis properties [12, 13], plasmonic properties for sensor applications [14, 15], biotechnological and biomedical applications [16, 17] supercapacitors [5], chemical energy actuator [18], and relatively high deformation capabilities [19, 20, 21]. More recently, the elaboration of ultra-thin film of nanoporous gold has been obtained through the dealloying of CuAu alloy [22]. These nanomeshes complete the zoology of nanoporous films obtained with other methods of elaboration as metal deposition [23], or metal

Email address: julien.godet@univ-poitiers.fr (Julien Godet)

nanowires [24]. Gold nanomeshes present high potential capabilities for flexible electronics [25, 26] due to their good properties of long range conductivity, high transmittance, and high stretchability [23]. Another promising application of these gold nanomeshes concerns molecular detection through the dramatic increase of the Raman scattering signal when molecules are absorbed on the surface [27]. These films detached from their initial glass substrate and floating on water can be transferred on the 3-dimensional surface of various substrates [22].

A previous experimental characterization of these ultra thin film materials revealed nanomeshes formed of very thin ligaments with cross sections of a few tens of nanometers, that can be considered as quasi two dimensional nanoporous films [22]. Here, we investigated ultra thin films of nanoporous gold using various microscopy approaches (Transmission Electron Microscopy (TEM), Scanning Electron Microscopy (SEM), and Atomic Force Microscopy (AFM)). The films are analyzed with numerical tools developed and optimized for these gold nanomeshes. Through the extraction of the skeleton, we determined the topology and geometry of the films at different length scales from nanometer to micron. A similar work has been completed in bulk nanoporous gold [28]. The statistical analysis on several length scales allows for a deep understanding of the gold nanomesh structure in view of future *in situ* mechanical investigations. It is also useful for generating realistic structures sourced from experiment samples for the purpose of atomic scale modeling. The first part presents the protocol of elaboration, the second the experimental analysis. The last part is dedicated to the quantitative statistical study of the properties of the nanoporous gold film.

2. Fabrication, preparation and characterizations

2.1. Protocol of fabrication

Ultra-thin nanoporous gold layers have been demonstrated to be transparent, conductive, and flexible membranes that can be transferred onto surfaces of complex shapes. A Cu film used as a sacrificial layer is first deposited onto a glass substrate, followed by thin layers of AuCu alloy (Fig. 1). The samples are then exposed to a nitric acid vapor which oxidizes copper into copper nitrate. This process has two effects: on the one hand, there is an etching of the sacrificial Cu layer that makes the membrane easily removable from the glass substrate; on the other hand, it performs the dealloying of copper from the CuAu alloy to obtain a nanoporous gold film. It should be noted that the use of an acid vapor instead of a solution is mandatory in order to avoid the complete destruction of the film during dealloying. The substrate is then immersed in ultrapure water to detach the nanoporous gold membrane which will float on the water surface. The membrane is then transferred to the object to be coated (Fig. 1).

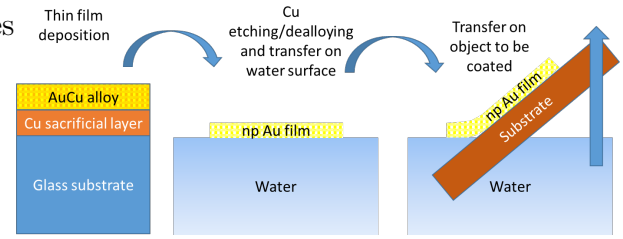

Figure 1: Fabrication and transfer of the highly flexible gold nanomesh ultra-thin film.

The thin films are deposited by magnetron cosputtering in argon plasma under a pressure of 0.5 Pa using gold and copper targets with a diameter of 75 mm. The target to substrate holder distance is about 120 mm. The initial sacrificial Cu layer is deposited with a DC power of 100 W applied to the target for 20 s. The thickness of this layer is deduced from previous calibrations performed by profilometry on thicker layers and is estimated to be 8 nm. The AuCu alloy layer is deposited with an average target power of 125 W for copper and 50 W for gold, with a deposition time of 10 s. The estimated thickness of this layer is 8 nm. The composition deduced from energy dispersive spectroscopy measurements on samples with higher layer thicknesses is estimated to be $Au_{35}Cu_{65}$. In a closed chamber, the samples are then subjected to nitric acid vapor for etching and dealloying. The vapor is produced from a concentrated nitric acid solution (65%, 16 mol.L^{-1} Carlo

Erba Reagents) at room temperature. The treatment time is 120 min. More details about the fabrication process can be find elsewhere [22]. In this study the produced membranes were transferred onto the surface of 3 types of substrates: a 300 mesh Cu grids coated with a lacey carbon film to perform TEM imaging, aluminum sample supports for SEM imaging, and Poly Ether Ether Ketone (PEEK) bar (2x2x6 mm^3) for AFM characterization.

2.2. Operating parameters for microscopy characterization

SEM Images are acquired using a Helios NanoLab G3 CX dual beam FIB/SEM machine from Thermofisher, equipped with a stage having free axes of rotation and tilt. Once a protective layer of platinum has been deposited, a rectangular hole on the surface of the sample is created by using the Ga^+ ion beam in order to access the cross-section view (fig. 3). Then, the sample is tilted at 38° relatively to the incident electron beam. The UHR (ultra-high resolution) SEM option, also known as the immersion mode, is used in order to obtain images with quality resolution at high magnifications (3kV, 0.34 nA). Top view images are obtained when the electron beam is perpendicular to the surface (Fig. 2).

TEM imaging was conducted with a S/TEM Themis Z G3 (300kV, Thermo Fisher Scientific).

All AFM observations were carried out in Peak Force Tapping mode on a Bruker Dimension Icon AFM with Bruker Scan Assist tips ($f_r \sim 70$ kHz, $k \sim 0,4$ N/m). PEEK substrates have been chosen for future deformation experiments because of its interesting physical and mechanical properties. Firstly, it is a semi-crystalline material with an elastic range up to 8% strain and a high Young modulus for a polymer (Es = 4.0 GPa) which gives it good rigidity. Secondly, water does not play a significant role in its elasticity unlike many other polymers, and does not affect its performance during the transfer of gold nanomesh.

2.3. PEEK Polishing process

PEEK 450GTM purchased from VictrexTM was cut into substrates of 2×2 mm^2 cross-section and 6 mm length. Each sample was mechanically polished using Mecatech 234 from Presi SA automatic polishing device. In the first polishing round, leveling of the sample surface is performed with Presi TOP, Reflex PAD-MAG polishing fabric for leveling of the sample surface. With a polishing time of 5 minutes and a force of 10 N, the polishing speed was set at 250 rpm, and diamond suspension of 10 µm grain size was intermittently supplied to the polishing pad. For the next polishing round, RAM, Reflex PAD-MAG polishing fabric and 3 µm diamond suspension were used with similar polishing parameters as in round one. The procedure was completed by using an NT, Reflex PAD-MAG polishing fabric, and 1/4 µm diamond suspension. The sample was thereafter cleaned in de-ionized water and dried in compressed air. This procedure leads to surfaces with a nanometer-scale corrugation.

3. Results of experimental characterizations

3.1. SEM / FIB

Figure 2 presents SEM images of nanoporous gold ultra-thin films at different scales. They reveal a relatively uniform nanomesh over a large area with lateral dimensions greater than 50 µm. The nanomesh includes pores of different sizes from a few tens of nanometers up to almost 2 µm. Interestingly, our observations reveal most of the time the presence of a unique sheet of gold nanomesh on the aluminum sample support which confirms the good control of the transfer process. The ligaments have a wavy shape, with diameters of 10 to 30 nm, independently of their location on the sample. Ligaments seem in general connected over a long scale, despite the presence of a few isolated clusters, as seen on the largest magnification image. This observation is in agreement with electrical percolation measurements performed previously on large sample [22]. Note that an EBSD analysis has been performed but the signal from the nanomesh was masked by that of the substrate.

Figure 3 reports on diameter dimensions, measured by taking into account the tilted angle ob-

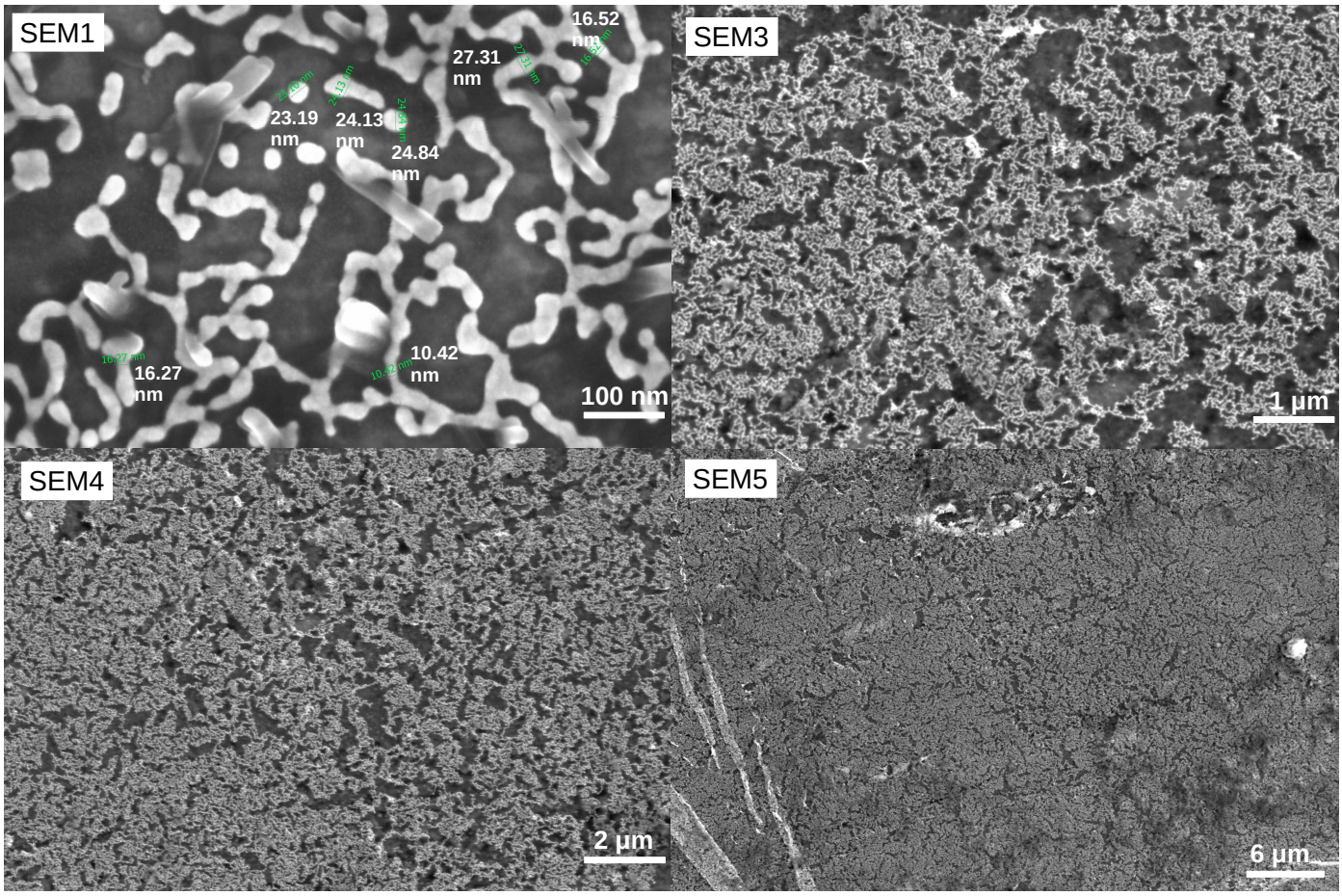

Figure 2: Top-view SEM images of gold nanomesh (light grey areas) at different length scales, with scale bars ranging from 100 nm to 6 μm. Labels SEM1, SEM3, SEM4, and SEM5 refer to Tab. 1 (For SEM2 see Fig. 6).

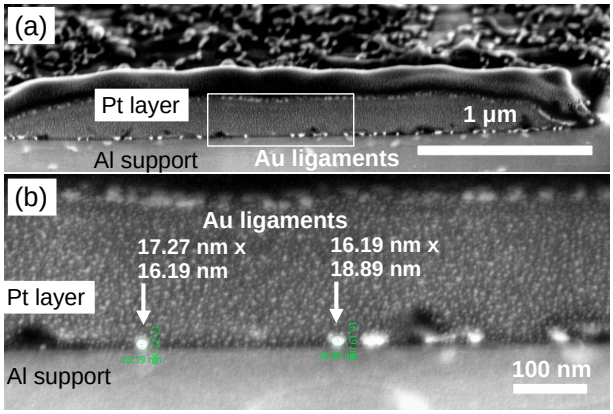

Figure 3: Gold ligaments cross section obtained by FIB milling on tilted surface are located at the interface between the Al layer of the aluminum sample support and the Pt protective layer. They appear in white. The diameters have been corrected to take into account the tilted angle observation. (a) Low magnification, (b) high magnification.

servation correction. Different cross section shapes, from almost circular to ovoid, are observed. The circular shape is attributed to the radial cross-section of ligaments, while the ovoid could be either radial or tilted cross-sections of ligaments. Circular cross sections are determined to range from about 16 to 19 nm, corresponding to the lower bound of the diameters estimated from the top view image (Fig. 3).

3.2. TEM

Information relatively similar to SEM analysis is obtained from TEM images (Fig.4) for ligaments shape, film structure, and pores. Note that the characteristic dimension of a pore is estimated to be about 200 nm (TEM1 in Fig.4). Larger pores, with dimensions that can reach 1 or 2 μm are also identified (TEM3 in Fig.4). The improved definition of TEM images compared to

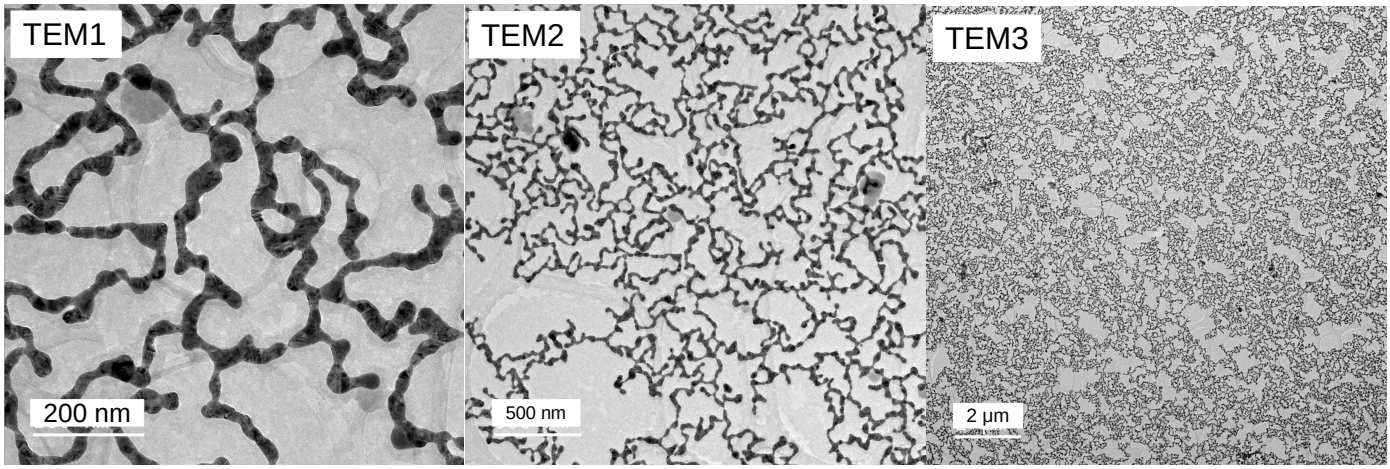

Figure 4: TEM images at different length scales, with scale bars ranging from 200 nm to 2 μm. The gold nanomesh corresponds to dark gray areas. Labels TEM1 to TEM3 refer to Tab. 1.

SEM allow us to better identify contours and also suggest planar structural defects that could be related to twinning, grain boundaries, or stacking fault defects.

3.3. AFM characterization

After transfer, the ligaments observed by AFM exhibit a similar organization compared to SEM and TEM observations. A typical image is shown in Fig. 5. It shows a relatively uniform single sheet of Au nanomesh with a variable density of gold ligaments. Profiles made across several ligaments give lateral dimensions between 35 and 55 nm and heights between 20 and 40 nm for ligaments. It can be noticed that the lateral dimensions measured by AFM are larger than the ones reported with the other methods. The two most important AFM tip-related factors that affect the quality of the AFM scans are the tip apex radius of curvature and the sidewall angles. The tip radius is the real limitation of the ultimate resolution for AFM measurements. Sidewall angles affect the accurate imaging of steep slopes. In the present work, tip specifications indicate a maximum radius of 12 nm, i.e. of the same order than the ligaments, hence the broadened features.

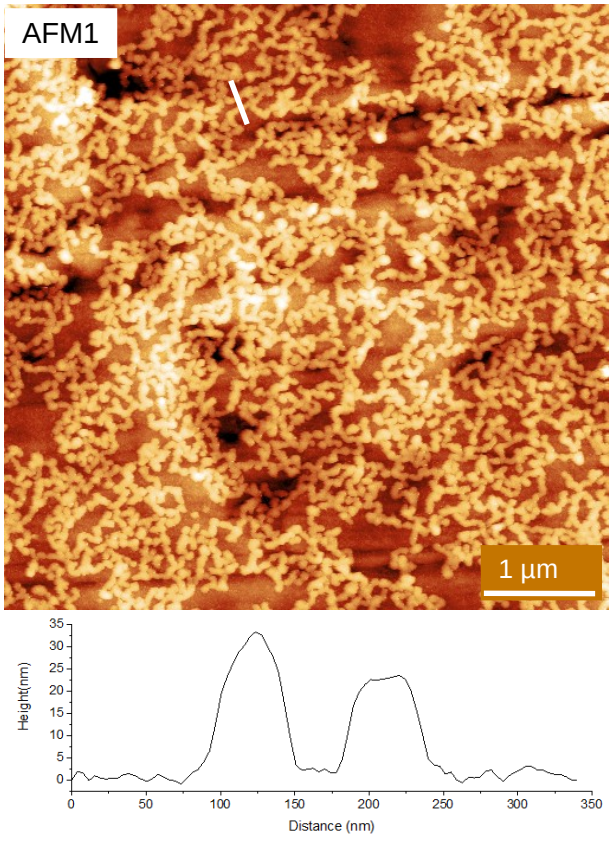

Figure 5: top image (AFM1) : AFM image of Au nanomesh. The bottom curve shows a typical profile across two ligaments and corresponds to the white bar in the top image.

4. Numerical analysis of the nanomesh

A comprehensive characterization of the nanomesh is relatively complex because the geometrical and topological properties are not uniform in the full film. A numerical analysis is then unavoidable to obtain good statistics. For such a structure, a useful primary step is the determination of the skele-

ton of the nanomesh, which can next be used to determine the continuity of the nanomesh and its topology and geometry. The skeleton is composed of ligaments and nodes. A ligament is a continuous gold wire linking two nodes or attached to a node at one of its end (end-free ligament). A node is defined as an intersection of three or more ligaments. From the skeleton analysis, several quantities can be extracted like the diameter, the length, and the connectivity of each ligament. In the following, the choice of the skeletonization algorithm and the methodology applied to limit possible artifacts generated by the skeletonization algorithm are presented.

4.1. Set up for skeleton evaluation

In order to analyze the gold nanomesh, we tested several skeletonization algorithms. Since these algorithms operate on black-and-white images, one critical step is the black-and-white binarization of experimental images (Fig. 6). Experimental images are first filtered until ligaments are clearly emphasized (Fig. 6c). Then a local threshold binarization is applied to finally obtain binary images. A particular attention has been taken during image processing to avoid blurring effects that could artificially change the apparent diameter of ligaments.

Several skeletonization methods are available, like those included in the 'Scikit-image' python library [29]. We compared two methods suited for the two dimensional analysis of microscopy images: the medial axis method and Zhang method [30]. The superiority of one method over the other mainly depends on the resolution of the binary input image and of the shape of the mesh. In our case, Zhang method has been selected because we found that the artifact ligaments potentially generated by this method can be efficiently removed by using the geometric criteria detailed below. A Python script largely inspired by the 'Aquami' software [31] has been written to refine the skeleton and to perform a statistical analysis of the gold nanomesh for determining the diameter, length, and orientation of ligaments.

4.2. Optimization of the skeleton: criteria to eliminate artifacts

The skeleton freshly calculated by the Zhang algorithm [30] features numerous small branches, such as those shown in blue circles in Fig. 6. These branches are artifacts produced by the algorithm, and are found at the proximity of wavy ligaments for example. To get a cleaned skeleton, these spurious branches are removed using several criteria. First, ligaments are classified according to their connectivity (Fig. 7). Ligaments with connectivity equal to 0 are not connected to the skeleton and are then rejected. In Fig. 6a, it represents about 1100 ligaments, almost one-third of the total, but counts only for 5.6 μm of the full cumulative length of 77 μm (Fig. 7b).

Pending ligaments are connected to the skeleton by one extremity only. They have a connectivity of one (blue bars labeled '1' in Fig. 7). Among them, a large part of the shortest ligaments are artifacts created by the skeletonization algorithm (blue circles in Fig. 6). Two criteria, the first based on diameter and the second based on length-over-diameter aspect ratio, are used for rejection in order to get a relevant gold nanomesh skeleton, as shown in red in Fig. 6d. The first criterion is controlled by the choice of the minimum diameter for the survival ligaments. Only ligaments with diameter larger than 0.3 times the average diameter of ligaments calculated on the full structure before rejection are conserved. This value allows to reject all the thinnest ligaments that have been identified as spuriously generated by the skeleton algorithm. The second criterion leads to the rejection of ligaments with a length-over-diameter aspect ratio of less than 1. In the chosen example, almost 300 additional ligaments with a connectivity of 1 are then rejected for a negligible cumulative length of 4.6 μm indicated by hashed blue bars in Fig. 7b, over the total length of 77 μm. Taken together, the total ligaments length is reduced by only 13% after skeleton cleaning.

This procedure is applied to all experimental images in this work and leads to a similar proportion of rejected ligaments. In the following, the statistical analysis are done on the cleaned skele-

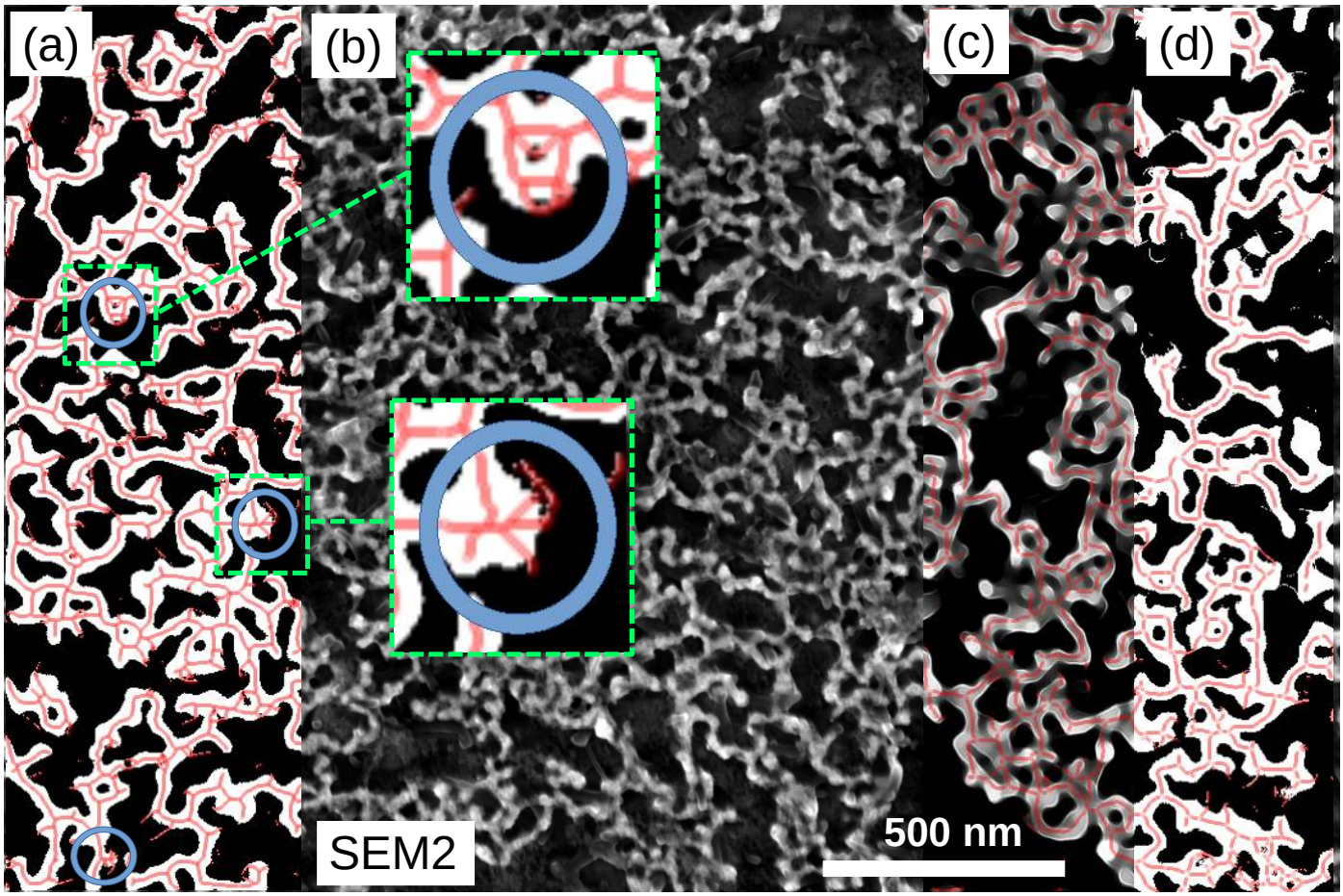

Figure 6: Processed images and skeleton superimposed on the experimental SEM image (SEM2). (a) skeleton as given by the skeletonization algorithm (red lines) on the black and white binarized image. (b) the background image is an experimental top-view SEM image labeled SEM2. Ligaments are gray on the experimental image and white on the binarized image. Blue circles denote skeleton artifacts magnified in zooms. (c) optimized skeleton (red lines) on the processed image. (d) optimized skeleton (red lines) on the black and white binarized image.

ton, after rejection of the spurious ligaments.

5. Results and discussion

5.1. Statistical analysis of gold nanomesh at various length scales

The microscopy characterizations are summarized in Tab. 1. The orientation of each ligament is calculated with respect to the horizontal axis of the film (Fig. 8a). All the ligaments orientations range from 0 to +90°, and with an average value close to 45 degrees. This means that ligaments are randomly orientated independently of the scale of observation, suggesting an isotropic structure of the thin films.

The average diameters range from 18 to 30 nm (Fig. 8b) for TEM and SEM. A slight increase in ligament diameter was observed with increasing length scale. However, this effect may be related to image post-processing. Effectively, at large length scales, the ligaments appear very thin with a loss of contour definition in the experimental images. The post-processing of the images may have resulted in the diameter being slightly too thick during image binarisation. The smallest sizes 18 to 22 nm are then probably the best average diameter evaluation in agreement with the SEM cross-section measurement (Fig. 3). The overestimation of the average diameter in AFM by about 25-30 nm is probably a consequence of the convolution of the ligament by the AFM tip as explained in section 3.3.

The average ligament length values are very

Table 1: Analysis of the skeleton calculated from experimental images at different scales, obtained with different characterization techniques. TEM images (green rows) correspond to Fig. 4, AFM image (blue row) to Fig. 5, SEM images (orange rows) to Fig. 2 and Fig. 6. The image are sorted by ascending value of their characteristic length scale, calculated as the square root of the image area. The ligament orientations are calculated with respect to the horizontal axis and range from 0 to +90°. An isotropic structure will then present an average orientation of +45°. The length density refers to the cumulative length of all ligaments divided by the image surface area. The opacity corresponds to the density of ligaments coverage, *i.e.* the percentage of surface occultation by ligaments on the full image.

image label	length scale (µm)	ligaments				opacity of the mesh	
		average orientation (deg)	average diameter (nm)	average length (nm)	Cumulative length (µm)	length density (µm/µm²)	over full image (%)
SEM1	0.7	43	22	50	9	20.9	30
TEM1	0.8	48	21	49	7	11.2	30
SEM2	2.3	46	23	36	67	13.2	43
TEM2	2.6	44	18	23	80	11.8	28
AFM1	5.0	44	52	117	134	5.3	39
SEM3	6.8	46	26	52	379	8.6	31
TEM3	13.5	45	30	66	1659	9.1	32
SEM4	13.6	50	30	82	1428	7.7	35
SEM5	44.7	-	-	-	-	-	37

scattered from 23 to 117 nm. For TEM and SEM images, at the smallest length scales, between 1 and 7 μm, the average ligament lengths are observed to be the smallest, whereas at the largest length scale the average ligament lengths appear to be the largest (Fig. 8c). AFM yields an average length of 117 nm (AFM1 in Fig. 8c), i.e. about 60 nm longer than for a similar scale image (SEM3 in Fig. 8c). A possible explanation hinges on the ligaments adhesion to the PEEK substrate that might improve the deposition and limit breaking.

Note that this overestimation of the average length has little impact on the cumulative lengths, that are independent of the techniques (AFM, SEM, or TEM), but only increase as a function of the length scale of the image (Tab. 1). In summary, at the largest length scale, the average ligament length could be seen as a converging value towards approximately 70 nm.

5.2. Opacity analysis of the nanomesh at different length scales.

The 'length density' is the ratio of the cumulative length over the surface area. In Fig. 8-d, at low length scale the values appear scatter, while at large length scale the values appear independent of the microscopy techniques. To explain this variation, we calculated the opacity of the nanomesh, that is the ratio of the white surface area representing ligaments over the full image area (Tab. 1). Careful image processing is required to correctly evaluate the opacity property (see the section 4.1). This property can also be understood as the product of the length density and the mean diameter. One can notice significant variations between all investigated samples, especially at a low length scale. To study the issue further, the opacity has been evaluated after the image is divided in 20 sub-images corresponding to a sampling of $1/20^{th}$ (5×4) of the full image. At the smallest scales, the scattering of opacity can vary by more than 20%, while at a larger length scale, the variations are about 2%. Furthermore, the standard deviation decreases from 5.4% to 0.7% when the length scale increases from 0.7 to 44.7 μm. In fact, the nanomesh can be viewed as clusters of densely nested ligaments connected by longer ligaments at a larger length scale, together with the presence of large pores in between (SEM4 in Fig. 2). When the lateral dimensions of images are larger than the largest pore size, of about 2 μm, the characteristics of the nanomesh appear then homogeneous and can explain the long-range percolation of the network previously observed by conductivity analysis [22].

5.3. Comparison with 3D bulk nanoporous gold.

In the work of Rösner et al. [32], bulk nanoporous gold has been elaborated from the dealloying of AgAu alloy and investigated by electron tomography. The conditions of elaboration lead to a

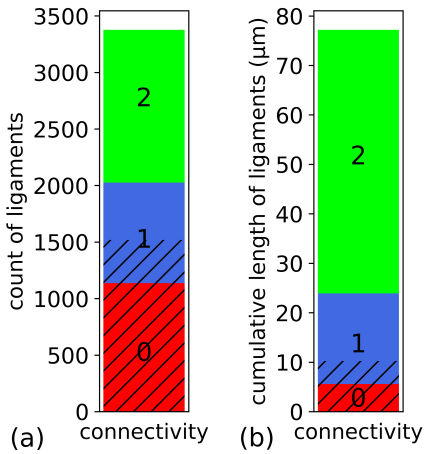

Figure 7: Example of ligaments analysis made on images shown in Fig. 6 before and after cleaning process, (a) in terms of number of ligaments, (b) in cumulative length (μm). In each plot, the ligaments are sorted according to their connectivity: 0 = free ligaments, 1 = one extremity connected to the skeleton, 2 = two extremities connected to the skeleton. The hashed zones represents rejected ligaments in number and in cumulative length. The subsequent statistical analysis is performed on skeletons after the rejection of the spurious ligaments. (See text for details).

bulk structure with an average ligament diameter of about 16 nm in bulk, i.e. close to our value of about 20 nm in our thin films. However, the average pore size of 28 nm in bulk nanoporous gold appears much smaller compared to the common pore diameter of about 200 nm, with a maximum of up to 2 μm observed in our gold nanomesh thin film. The reduction in pore size in the transition from 2D to 3D nanoporous films is also observed, for example, in the analysis of nanoporous metallic films obtained by other means, where the same issues are addressed by molecular dynamics [33] and Langevin-based modelling [34] in terms of the slice-filling factor. This raises the question of whether this trend could be common to all nanoporous metallic films, however synthesised, in the transition from the 2D to the 3D case. However, this requires more detailed studies.

Interestingly, the stability of ligaments in films is in agreement with the Plateau-Rayleigh instability calculated on a cylinder with surface tension as in the bulk structures [32]. In fact, the ratio of the average length to the average diameter is always smaller than π, which limits instability leading to the pinch-off of thin ligaments. The stability of nanoporous gold seems not affected by the lowering of space dimension from bulk to quasi-2D ultra-thin film. However, the mechanical properties of the films could be strongly impacted due to the presence of much larger pores than in the bulk structures. It could explain the large strains up to 160% reported for certain nanomeshes [23] while bulk nanoporous gold with similar ligaments diameter is brittle [35].

6. Conclusion

To conclude, the analysis at different length scales reveals a homogeneous and isotropic topology of the nanomesh at a length scale larger than the maximum pore diameter of about 2 μm. The nanomesh presents local variations of ligament density, with nested ligaments connected by longer ligaments. In addition, TEM and SEM characterizations lead to similar average values of about 20 nm for the ligaments diameters, and of about 70 nm for the ligaments length, while AFM overestimates those properties. The topology of the nanomesh is not affected by the AFM tip convolution effect. AFM could then be used like TEM and SEM to study the topology modification in view of future investigations about mechanical properties. We also find that the opacity of the nanomesh converges toward a relatively constant value of about 35% at a large enough length scale. Finally, the algorithm developed in this study gives a precise description of the quasi-2D topology and could be used for other quasi-2D nanomaterials such as percolated silver nanowires for transparent conductor electrode [24].

TEM observations also reveal defects in ligaments, and call for further research, for instance using the Automated Crystal Orientation Mapping in Transmission Electron Microscope (ACOM-TEM) tool [36]. This would help us to study the crystalline orientation of the ligaments at the nanoscale.

The presence of much larger pores in gold nanomesh thin films than in gold nanoporous bulk should

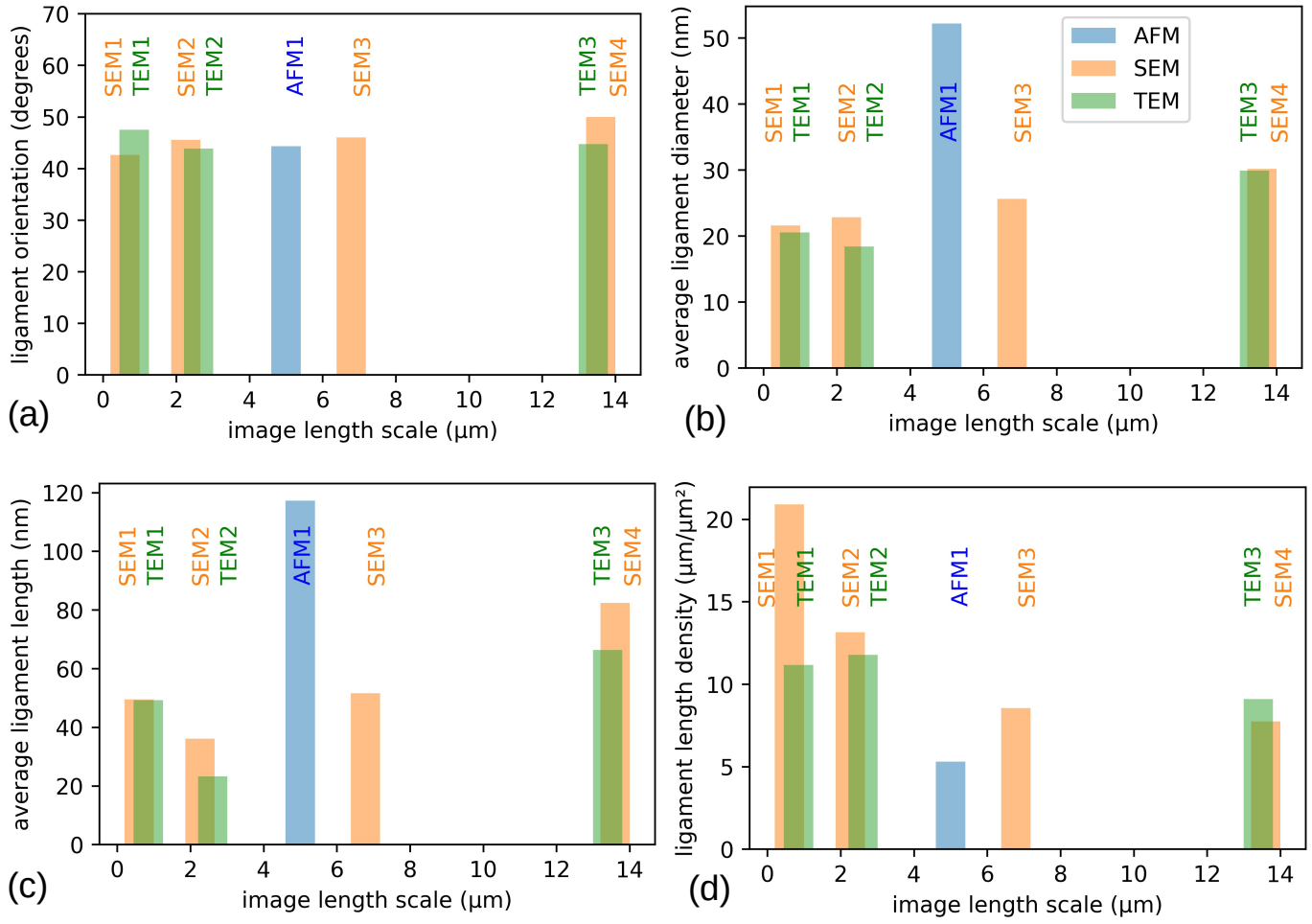

Figure 8: Statistical representation of data from Tab. 1. (a) ligament orientation (°), (b) average ligament diameter (nm), (c) average ligament length (nm), and (d) ligament length density (μm/μm^2). Orange, green and blue bars are respectively for SEM, TEM and AFM experimental images.

affect the evolution of topology and connectivity during mechanical deformation. The consequence of the modification of the morphology of nanoporous gold from bulk to quasi-2D ultra-thin film on mechanical properties like ductility should then be investigated. One goal would be to determine the limit of such metallic nanomesh and the engineering way to improve their mechanical properties for subsequent applications.

Acknowledgements

This work pertains to the French Government programs "Investissements d'Avenir" EUR INTREE, reference ANR-18-EURE-0010, and LABEX INTERACTIFS, reference ANR-11-LABX-0017-01. The Authors greatly acknowledge the Funding by the French Contrat Plan État-Région, the European Regional Development Fund of Pays de la Loire, the CIMEN Electron Microscopy Center in Nantes, the Région Pays de la Loire, France - RFI WISE - ORCAP Project, and the Programme de prématuration 'Membranes d'or nanomaillées' CNRS, France.

References

[1] M. F. Ashby, Materials Selection in Mechanical Design (Fourth Edition), fourth edition ed., Butterworth-Heinemann, Oxford, 2011. doi:https://doi.org/10.1016/B978-1-85617-663-7.00026-6.

[2] G. Benetti, F. Banfi, E. Cavaliere, L. Gavioli, Mechanical properties of nanoporous metallic ultrathin films: A paradigmatic case, Nanomaterials 11 (2021) 3116. doi:10.3390/nano11113116.

[3] R. O. Ritchie, The conflicts between strength and toughness, Nat. Mater. 10 (2011) 817–822. doi:10.1038/NMAT3115.

[4] J. Weissmüller, R. C. Newman, H.-J. Jin, A. M. Hodge, J. W. Kysar, Nanoporous metals by alloy corrosion: Formation and mechanical properties, MRS Bulletin 34 (2009) 577–586. doi:10.1557/mrs2009.157.

[5] T. Juarez, J. Biener, J. Weissmueller, A. M. Hodge, Nanoporous metals with structural hierarchy: A review, Adv. Eng. Mater. 19 (2017). doi:10.1002/adem.201700389.

[6] X. Lu, T. Balk, R. Spolenak, E. Arzt, Dealloying of Au-Ag thin films with a composition gradient: Influence on morphology of nanoporous Au, Thin Solid Films 515 (2007) 7122–7126. doi:https://doi.org/10.1016/j.tsf.2007.03.023.

[7] X. Wang, Z. Zhang, H. Ji, J. Xu, X. Huang, Y. Ma, Dealloying of single-phase Al_2Au to nanoporous gold ribbon/film with tunable morphology in inorganic and organic acidic media, Appl. Surf. Sci. 258 (2012) 9073–9079. doi:https://doi.org/10.1016/j.apsusc.2012.05.165.

[8] Y. Wang, J. Xu, B. Wu, Chloride ion effect and alloying effect on dealloying-induced formation of nanoporous AuPt alloy, Appl. Surf. Sci. 276 (2013) 262–268. doi:https://doi.org/10.1016/j.apsusc.2013.03.080.

[9] D. Wang, J. Ihlemann, P. Schaaf, Complex patterned gold structures fabricated via laser annealing and dealloying, Appl. Surf. Sci. 302 (2014) 74–78. doi:https://doi.org/10.1016/j.apsusc.2013.12.066.

[10] Y.-Z. Lee, W.-Y. Zeng, I.-C. Cheng, Synthesis and characterization of nanoporous copper thin films by magnetron sputtering and subsequent dealloying, Thin Solid Films 699 (2020) 137913. doi:https://doi.org/10.1016/j.tsf.2020.137913.

[11] W.-H. Tsai, C.-H. Tang, I.-C. Cheng, The mechanical and catalytic behavior of nanoporous copper film on octet-truss lattice via magnetron sputtering, Thin Solid Films 724 (2021) 138628. doi:https://doi.org/10.1016/j.tsf.2021.138628.

[12] T. Fujita, P. Guan, K. McKenna, X. Lang, A. Hirata, L. Zhang, T. Tokunaga, S. Arai, Y. Yamamoto, N. Tanaka, Y. Ishikawa, N. Asao, Y. Yamamoto, J. Erlebacher, M. Chen, Atomic origins of the high catalytic activity of nanoporous gold, Nat. Mater. 11 (2012) 775–780. doi:10.1038/NMAT3391.

[13] S. Qin, Y. Liu, S. Liu, X. Wang, Y. Li, C. Qin, Z. Wang, M. Li, Self-standing porous Au/CuO nanowires with remarkably enhanced visible light absorption and photocatalytic performance, Appl. Surf. Sci. 594 (2022) 153443. doi:https://doi.org/10.1016/j.apsusc.2022.153443.

[14] J. Huang, Z. He, Y. Liu, L. Liu, X. He, T. Wang, Y. Yi, C. Xie, K. Du, Large surface-enhanced raman scattering from nanoporous gold film over nanosphere, Appl. Surf. Sci. 478 (2019) 793–801. doi:https://doi.org/10.1016/j.apsusc.2019.01.187.

[15] D. Raj, M. Palumbo, G. Fiore, F. Celegato, F. Scaglione, P. Rizzi, Sustainable nanoporous gold with excellent SERS performances, Mater. Chem.Phys. 293 (2023) 126883. doi:https://doi.org/10.1016/j.matchemphys.2022.126883.

[16] J. V. D. Zalm, S. Chen, W. Huang, A. Chen, Review—recent advances in the development of nanoporous Au for sensing applications, J. Electrochem. Soc. 167 (2020) 037532. doi:10.1149/1945-7111/ab64c0.

[17] F. Ruffino, M. G. Grimaldi, Nanoporous gold-based sensing, Coatings 10 (2020). doi:10.3390/coatings10090899.

[18] J. Biener, A. Wittstock, L. A. Zepeda-Ruiz, M. M. Biener, V. Zielasek, D. Kramer, R. N. Viswanath, J. Weissmüller, M. Bäumer, A. V. Hamza, Surface-chemistry-driven actuation in nanoporous gold, Nat. Mater. 8 (2009). doi:https://doi.org/10.1038/nmat2335.

[19] D. Farkas, A. Caro, E. Bringa, D. Crowson, Mechanical response of nanoporous gold, Act. Mater. 61 (2013) 3249–3256. doi:10.1016/j.actamat.2013.02.013.

[20] H.-J. Jin, L. Kurmanaeva, J. Schmauch, H. Roesner, Y. Ivanisenko, J. Weissmueller, Deforming nanoporous metal: Role of lattice coherency, Act. Mater. 57 (2009) 2665–2672. doi:10.1016/j.actamat.2009.02.017.

[21] M. Guillotte, J. Godet, L. Pizzagalli, A fully molecular dynamics-based method for modeling nanoporous gold, Comp. Mater. Sci. 161 (2019) 135–142. doi:https://doi.org/10.1016/j.commatsci.2019.01.042.

[22] A. Chauvin, W. T. C. Heu, J. Buh, P.-Y. Tessier, A.-A. El Mel, Vapor dealloying of ultra-thin films: a promising concept for the fabrication of highly flexible transparent conductive metal nanomesh electrodes, NPJ Flexible Electronics 3 (2019). doi:10.1038/s41528-019-0049-1.

[23] C. F. Guo, T. Sun, Q. Liu, Z. Suo, Z. Ren, Highly stretchable and transparent nanomesh electrodes made by grain boundary lithography, Nat. Commun. 5 (2014). doi:10.1038/ncomms4121.

[24] C. F. Guo, Z. Ren, Flexible transparent conductors based on metal nanowire networks, Mater. Today 18 (2015) 143–154. doi:10.1016/j.mattod.2014.08.018.

[25] D. J. Lipomi, Z. Bao, Stretchable, elastic materials and devices for solar energy conversion, Energy Environ. Sci. 4 (2011) 3314–3328. doi:10.1039/C1EE01881G.

[26] S. Xiao, S. Wang, X. Wang, P. Xu, Nanoporous gold: A review and potentials in biotechnological and biomedical applications, Nano Select 2 (2021) 1437–1458. doi:https://doi.org/10.1002/nano.202000291.

[27] I. Shahine, J.-Y. Mevellec, M. Richard-Plouet,

B. Humbert, P.-Y. Tessier, Nanoporous gold stacked layers as substrates for SERS detection in liquids or gases with ultralow detection limits and long-term stability, J. Phys. Chem. C 126 (2022) 17223–17233. doi:10.1021/acs.jpcc.2c05903.

[28] E. T. Lilleodden, P. W. Voorhees, On the topological, morphological, and microstructural characterization of nanoporous metals, MRS Bull. 43 (2018) 20–26. doi:10.1557/mrs.2017.303.

[29] S. Van Der Walt, J. L. Schönberger, J. Nunez-Iglesias, F. Boulogne, J. D. Warner, N. Yager, E. Gouillart, T. Yu, the scikit-image contributors, scikit-image: image processing in Python, PeerJ 2 (2014) e453. doi:10.7717/peerj.453.

[30] T. Y. Zhang, C. Y. Suen, A fast parallel algorithm for thinning digital patterns, Communications of the ACM 27 (1984) 236–239. doi:10.1145/357994.358023.

[31] J. Stuckner, K. Frei, I. McCue, M. J. Demkowicz, M. Murayama, AQUAMI: An open source python package and GUI for the automatic quantitative analysis of morphologically complex multiphase materials, Comp. Mater. Sci. 139 (2017) 320–329. doi:10.1016/j.commatsci.2017.08.012.

[32] H. Roesner, S. Parida, D. Kramer, C. A. Volkert, J. Weissmueller, Reconstructing a nanoporous metal in three dimensions: An electron tomography study of dealloyed gold leaf, Adv. Eng. Mater. 9 (2007) 535–541. doi:10.1002/adem.200700063.

[33] G. Benetti, C. Caddeo, C. Melis, G. Ferrini, C. Giannetti, N. Winckelmans, S. Bals, M. J. Van Bael, E. Cavaliere, L. Gavioli, F. Banfi, Bottom-up mechanical nanometrology of granular Ag nanoparticles thin films, The Journal of Physical Chemistry C 121 (2017) 22434–22441. doi:10.1021/acs.jpcc.7b05795.

[34] N. Nasiri, T. D. Elmøe, Y. Liu, Q. H. Qin, A. Tricoli, Self-assembly dynamics and accumulation mechanisms of ultra-fine nanoparticles, Nanoscale 7 (2015) 9859–9867. doi:10.1039/C5NR00877H.

[35] R. Li, K. Sieradzki, Ductile-brittle transition in random porous Au, Phys. Rev. Lett. 68 (1992) 1168–1171. doi:10.1103/PhysRevLett.68.1168.

[36] E. Rauch, M. Véron, Automated crystal orientation and phase mapping in TEM, Mater. Charact. 98 (2014) 1–9. doi:https://doi.org/10.1016/j.matchar.2014.08.010.